Supplementary information

Cu nanoparticle-carbon nanofiber stabilized over pelletized biochar for catalytic wet air oxidation of Tetracycline under mild operating conditions

Shreerang Mishra[1], Rahul Gupta[1], Nishith Verma[1,2*]

[1]*Department of Chemical Engineering, Indian Institute of Technology Kanpur, Kanpur 208016, India.*

[2]*Center for Environmental Science and Engineering, Indian Institute of Technology Kanpur, Kanpur 208016, India.*

*Corresponding author: Prof. Nishith Verma
Tel: 91-512-259-6767, Fax: 91-512-259-0104
E-mail id: nishith@iitk.ac.in, vermanishith@gmail.com

S1. Materials and methods

S1.1. Materials

Tetracycline ($C_{22}H_{24}N_2O_8 \cdot HCl$, TC) (95%) was purchased from Sisco Research Laboratories Pvt. Ltd., Mumbai, (India). Bamboo shoots (*Bambusa vulgaris*) were acquired from the nursery at the Indian Institute of Technology Kanpur, Kanpur (India). HPLC grade acetonitrile and phenol (99%) was purchased from Merck Life Science Pvt. Ltd., Mumbai (India). Cupric nitrate trihydrate ($Cu(NO_3)_2 \cdot 3H_2O$, 99%) and HPLC grade water was purchased from Thermo Fischer Scientific, Nagpur (India). High-purity nitrogen (N_2), air, hydrogen (H_2), and acetylene (C_2H_2) gases were purchased from Sigma Gases, Delhi (India). All solutions were prepared in ultrapure water (Elix® Milli Q system, USA).

S1.2. Physicochemical characterization

The metal (Cu) loading in the prepared biochar pellets was determined by the atomic absorption spectroscopic (AAS, Varian AA-420, USA) analysis of the aqua regia-treated leachate solution. The metal loading (mg g^{-1}) in Cu-CNF/biochar(P) was determined by first crushing a single pellet to powder using a mortar-pestle. Next, 100 mg of the powdery material was mixed in 10 mL aqua-regia at 80 $^{\circ}$C and the mixture was placed in a fume-hood for five days at the same temperature. The resulting leachate was diluted with water and the samples were tested for the metal loading using the AAS analysis. AAS analysis was also used to determine the metal leaching, if any, in the residual TC solution post cWAO reaction. The surface morphology of the materials was observed using field emission scanning electron microscopy (FESEM, MIRA3 TESCAN, USA at 10 kV). Energy dispersive X-ray (EDX, JSM-7100F JEOL, USA) spectroscopy was used to determine the surface elemental compositions of the materials. The internal morphology of the materials was observed using transmission electron microscopy (TEM, FEI- Tecnai G2 12 Twin,

USA). The crystal planes in the materials were determined using X-ray diffraction (XRD, X'pert Pro PANalytical, USA). Fourier transform infrared (FTIR, Bruker Tensor 27, Germany) spectroscopy was used to identify the surface groups. The specific surface area and N_2 adsorption-desorption isotherms of the material were determined by the multi-point Brunauer–Emmett–Teller analysis (BET, Autosorb 1-C Quantachrome, USA). The thermal stability of the materials was assessed by thermogravimetric analyzer (TGA, Toledo-Mettler, USA). The graphitic content in the materials was determined by Raman spectroscopy (Alpha 300R Witec, Germany). X-ray photoelectron spectroscopy (XPS, K-th PHI 5000 Versa Prob II, FEI Inc., USA) was used to determine the surface oxidation state of the elements in the material. The compressive strength of the prepared pellets was determined using universal testing machine (UTM, Tinius Olsen, USA). Electron impedance spectroscopy (EIS) was used to determine resistance to the electron transfer at the catalyst-reactive media interface on an electrochemical workstation (AUTOLAB-PGSTAT-302 N, Netherlands). Electron paramagnetic resonance (EPR) were performed using JEOL (JES-FA200) spectrometer to detect the reactive oxygen species.

S1.3. cWAO reactor assembly

TC degradation tests were performed in a cylindrical Inconel reactor (72 mm dia × 210 mm height × 8 mm thickness). Fig. S1 shows the digital photograph and schematic of the cWAO reactor used in this study. The reactor contained 1.5 kW-heating coils and a water-cooling jacket. A PID controller was used for temperature control. The reaction mixture was stirred using a catalyst-holder cum impeller fabricated specifically from stainless steel (SS). The catalyst holder had three horizontal sections separated by SS mesh. The walls of the catalyst-holder were perforated, allowing the easy flow of liquid through the catalyst bed. The catalyst-holder was fastened to the stem of the stirrer. The stirring rate was controlled using a motor with a variable

speed regulator. A pressure gauge was used to monitor the reactor pressure. A vent valve was installed at the reactor top for safety and/or purging purpose for releasing any excess pressure, or for cleaning the reactor. In a common experiment, the vent valve remained closed during the entire operation (oxidation reaction). The reactor-top head assembly was sufficiently tightened to prevent any leakage. Gas purifiers were installed in all supply lines to eliminate any moisture present in the gas.

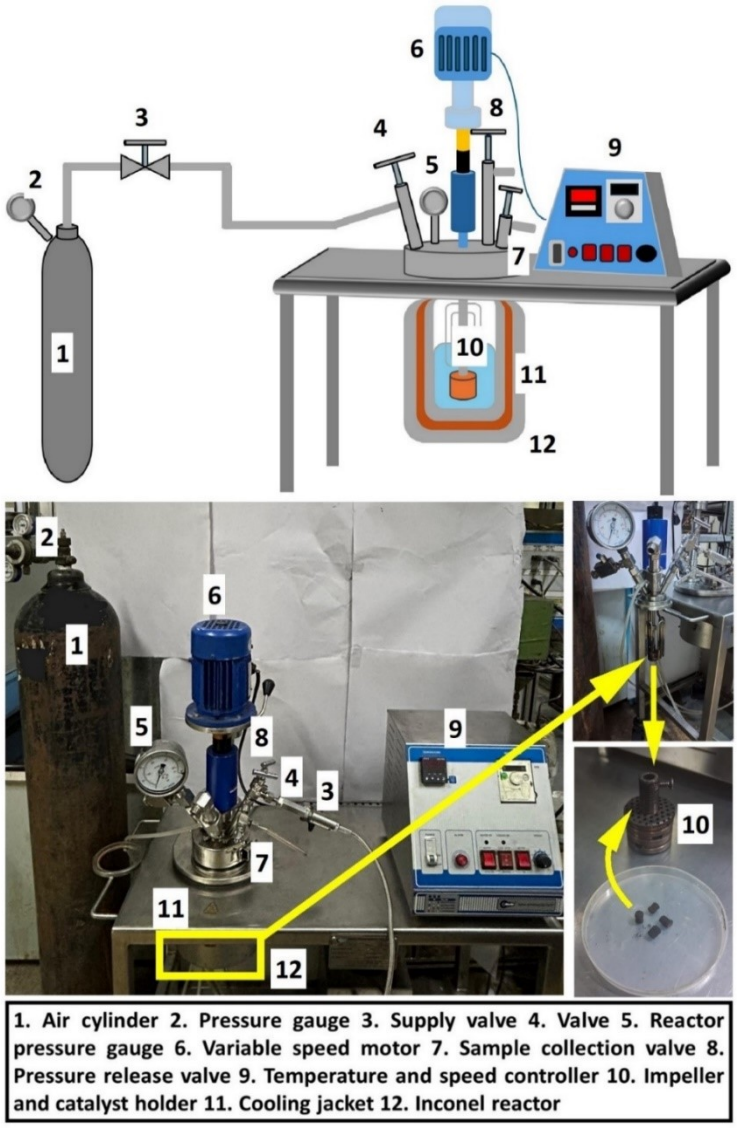

Fig. S1. Schematics and digital photograph of the cWAO reactor setup.

S1.4. TC analysis

A UV-Vis spectrophotometer (UV-Vis, Varian, Cary 100, USA) was used to determine the TC concentration in the filtered test samples, at a wavelength of 360 nm. A high-performance liquid chromatography (HPLC, Varian, Pro Star 210) equipped with a 250 mm × 4.6 mm reverse phase C18 column was used to determine the formation of any intermediates during the cWAO tests. The measurements or detection were carried out at 260 nm-wavelength, with the mobile phase consisting of 40 and 60% acetonitrile and HPLC water (with 0.1% formic acid), respectively at a flow rate of 1 mL/min. Closed-reflux titrimetric method was used to determine the COD of the treated samples. Hydrochloric acid reagents and the standard potassium dichromate solution (0.017 M) were used to digest the test run samples at 150 °C for 2 h. After cooling the digested samples to room temperature (~30 ^{o}C), ferrous ammonium sulphate solution (0.1 M) was used for titration. TOC in the spent solutions was determined using a TOC analyzer (Shimadzu, Japan 5050).

S2. Results and discussion

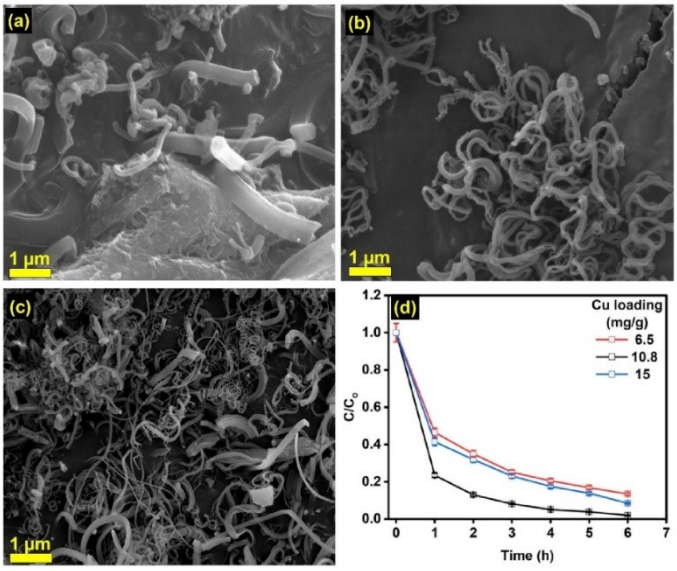

Fig. S2. CNF growth on the biochar substrate for varying Cu-salt amounts: (a) 1 g –growth with non-uniform fiber size, and lump formation, (b) 1.5 g – adequate growth, and (c) 2 g – growth with non-uniform fiber size, and (d) TC degradation tests at three different Cu-loading (initial

concentration = 100 ppm, catalyst dose = 1 g L^{-1}, pH = 4, temperature = 100 °C, pressure = 2 bar, stirrer speed = 250 rpm).

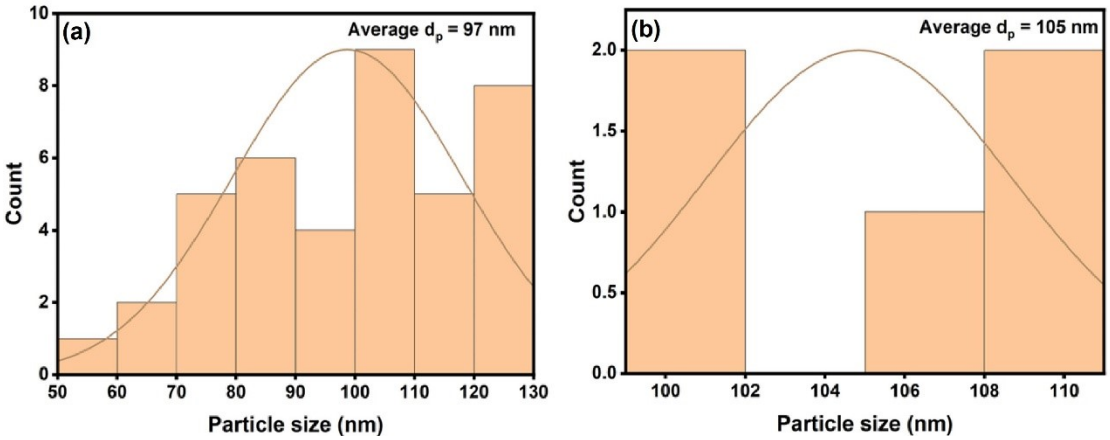

Fig. S3. Particle size distribution of the CNFs determined from (a) SEM and (b) TEM analysis.

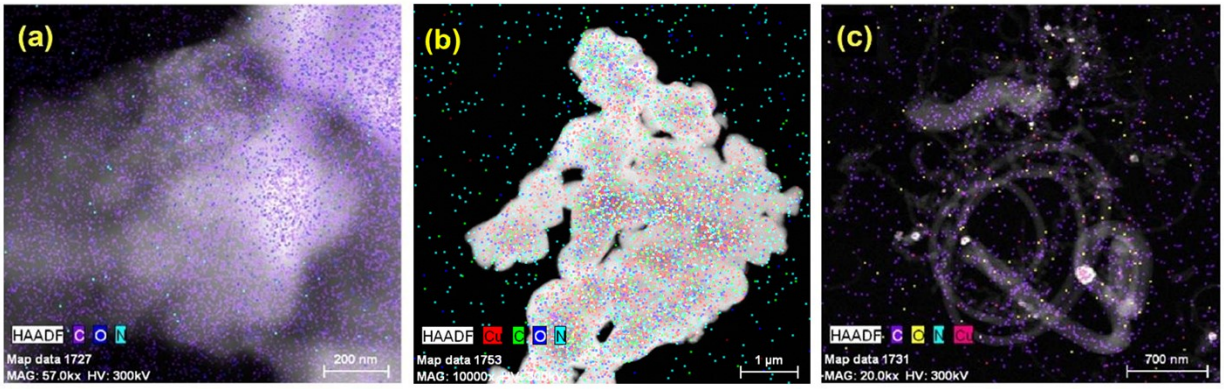

Fig. S4. HRTEM-EDS elemental mapping of (a) biochar, (b) Cu-biochar, and (c) Cu-CNF/biochar.

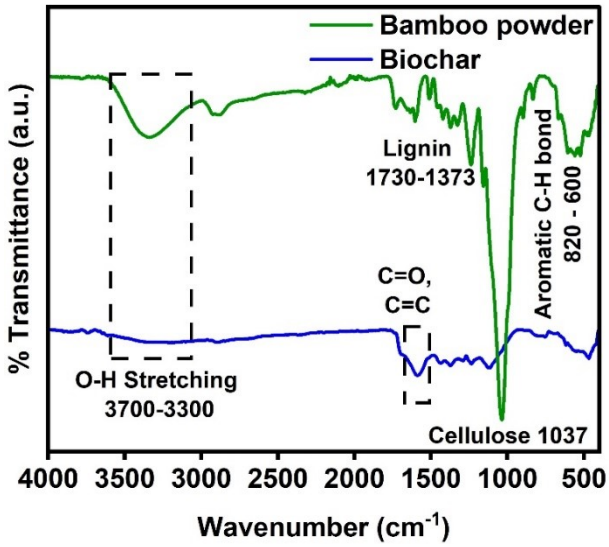

Fig. S5. FTIR spectra of Bamboo powder showing the characteristic peaks of lignin and cellulose.

Fig. S6(a-e) presents the XPS survey plot along with the corresponding spectra of C 1s, N 1s, O 1s, and Cu 2p in Cu-CNF/biochar. The survey spectrum confirms the presence of C, O, N, and Cu in the synthesized material (Fig. S6a). The deconvolution of the C 1s spectrum shown in Fig. S5b reveals peaks at 284.45, 285.05, and 285.95 eV, attributed to graphitic C (sp^2-C), amorphous C (sp^3-C), and C-O/C-N, respectively[1]. The sp^2 hybridized carbon corroborates the presence of CNFs over the biochar surface, confirming the CNFs growth catalyzed by Cu. Fig. S6c shows deconvoluted N 1s curve confirming the presence of peaks at 397.85, 399.07 and 401.12 eV corresponding to pyridinic N, pyrrolic N, and graphitic N, respectively[2]. Fig. S6d shows the O 1s spectrum. The peaks at 531.8, 532.78, 533.8, and 534.05 eV are attributed to C=O, C-OH, C-C=O, and C-O-C, respectively[3]. Such oxygen-containing groups of different binding energies play a vital role in the generation of ROS for the oxidation reactions. The deconvoluted Cu 2p spectrum in Fig. S6e shows the characteristic peaks at 933.35 and 953.3 eV, corresponding to the Cu^0 or zero-valent Cu[4]. The zero-valent state indicates the potential of the metal to change to higher oxidation levels during the oxidation step and generate ROS that are critical for the oxidation reactions.

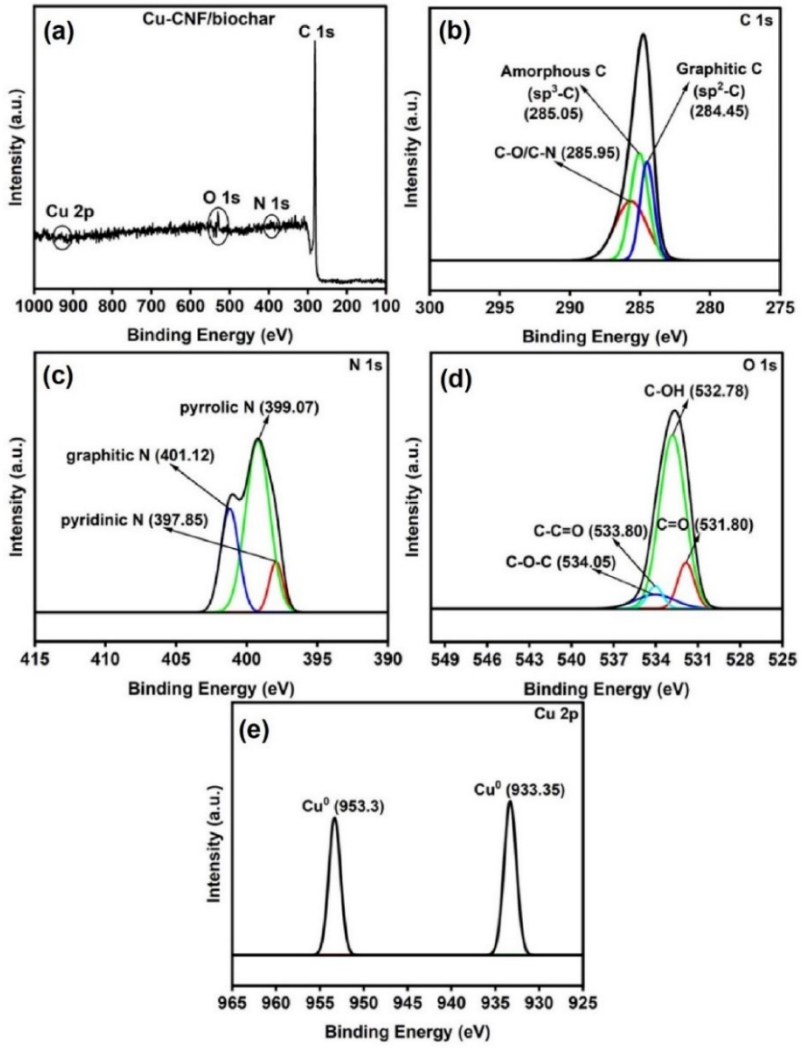

Fig. S6. (a-e) XPS spectra of Cu-CNF/biochar and the constituent elements.

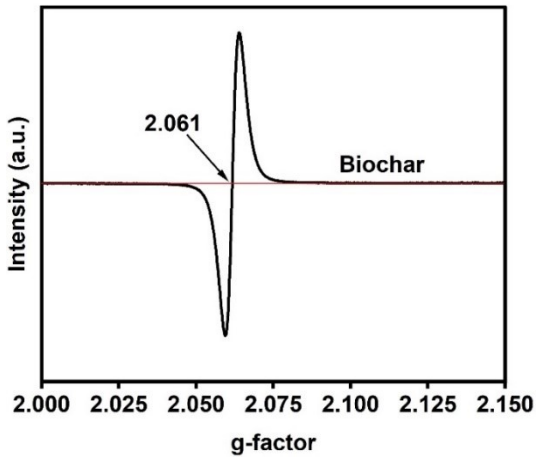

Fig. S7. EPR spectra for biochar (solid sample) used to confirm the EPFRs.

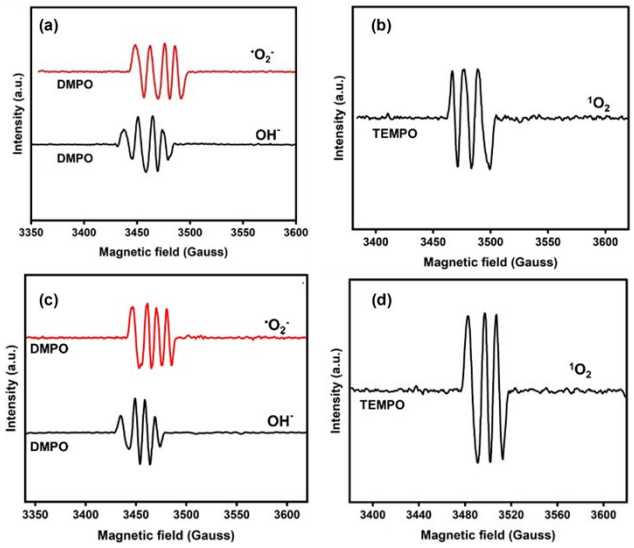

Fig. S8. EPR spectra of •OH, $•O_2^-$, and $^1O_2$ for (a-b) Biochar and (c-d) Cu-biochar.

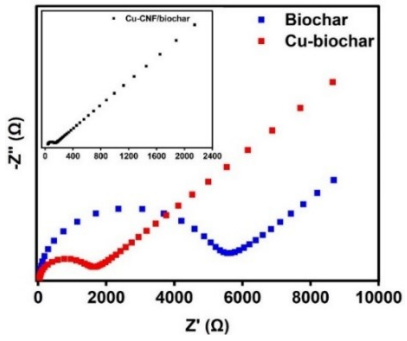

Fig. S9. EIS spectra of the materials used to compare the resistances to electron transfer.

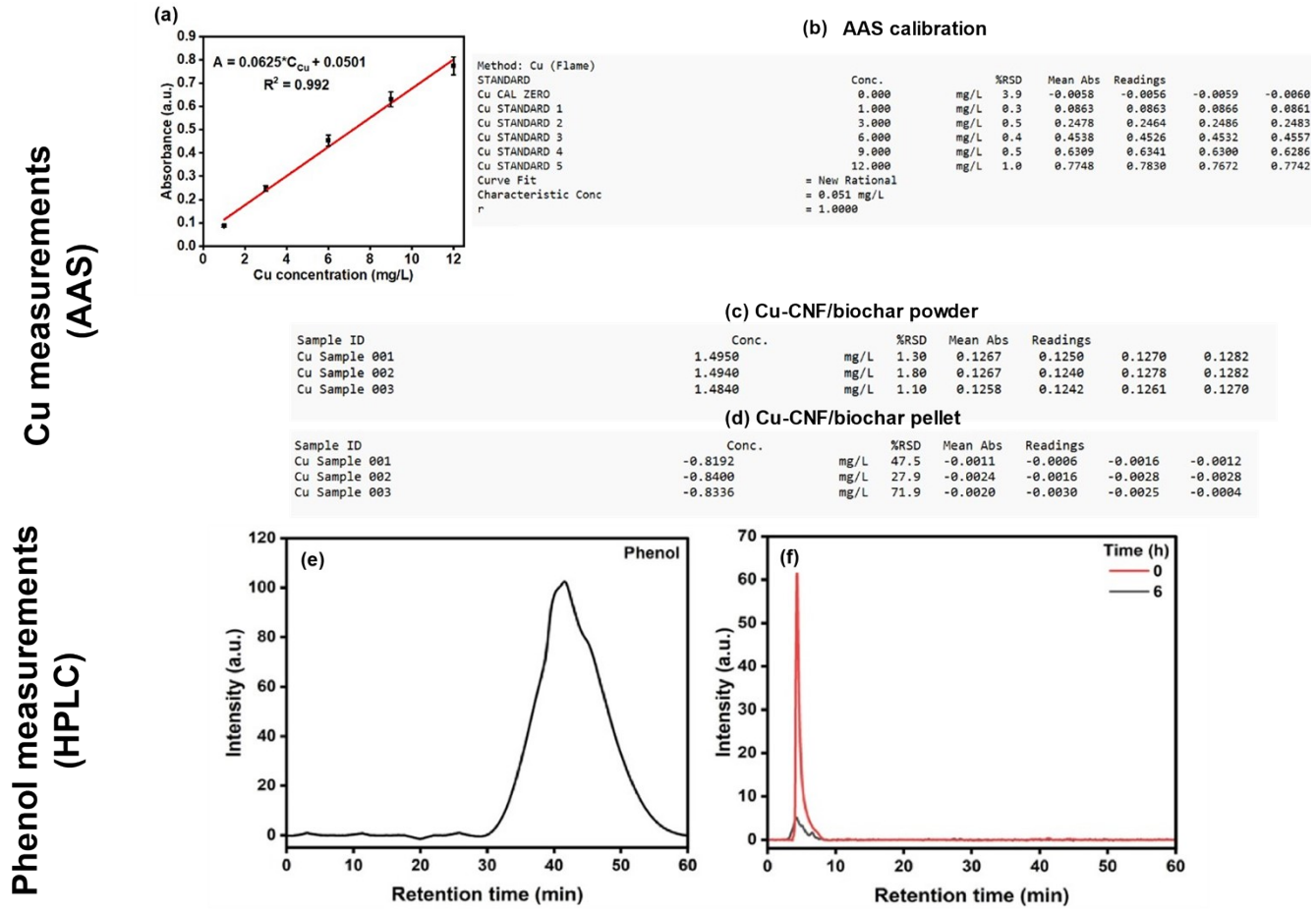

Fig. S10. (a) Calibration curve showing AAS absorbance vs. Cu concentrations (mg L^{-1}); (b) absorbance readings for the standard Cu solutions used for the calibration of the AAS instrument; AAS absorbance readings for samples collected post-6 h cWAO experiment using Cu-CNF/biochar: (c) powder and (d) pellet; HPLC chromatogram for (e) aqueous solution of 150 ppm phenolic resin; (f) initial and final samples from the TC activity tests. No peak of phenolic resin was detected in the TC activity test solutions.

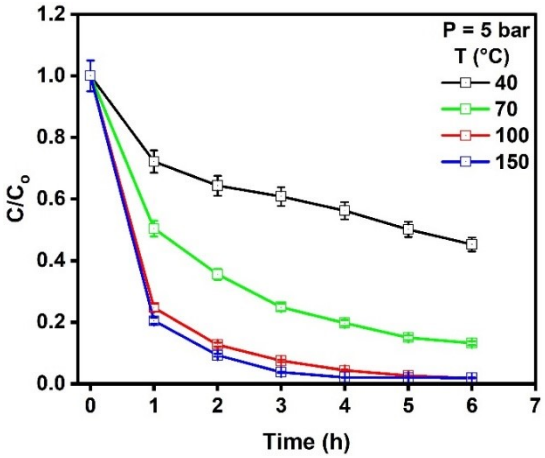

Fig. S11. Effect of temperature on TC degradation at the constant pressure of 5 bar (initial concentration = 100 ppm, catalyst dose = 1 g L^{-1}, pH = 4, stirrer speed = 250 rpm).

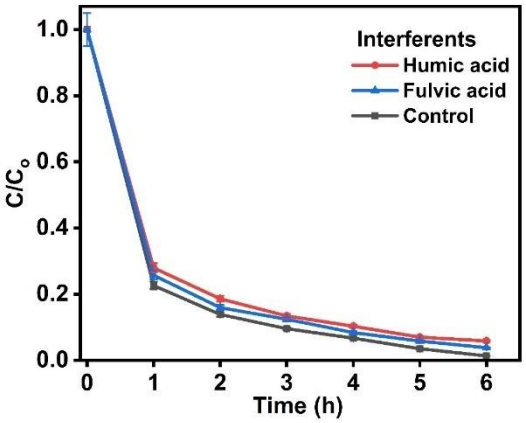

Fig. S12. TC concentration profile in the presence of humic and fulvic acid interferents.

Fig. S13a shows the effect of impeller speed on the degradation rate. The rate increased with the increasing speeds. The conversion increased from 90 to 99% in 6 h with the increase in the speed from 50 to 250 rpm. No significant increase in TC conversion was observed with the increase in the speed from 250 to 500 rpm, indicating that the degradation rate was not limited by the intra-particle mass transfer rate at the impeller speeds greater than 250 rpm. Table S1 shows the calculated values for the mass-transfer coefficients at different stirrer speeds. The next degradation tests were performed at 250 rpm.

BET area analysis has clearly shown the development of a porous substrate (biochar) (S_{BET} ~245 m^2 g^{-1}) as well as the biochar-supported catalyst (S_{BET} ~197 m^2 g^{-1}) in this study (Table 1).

Therefore, the decrease in TC concentration at the relatively lower temperatures by adsorption may not be ruled out. Therefore, adsorption tests were performed at 30 (1 bar) and 100 °C (2 bar)

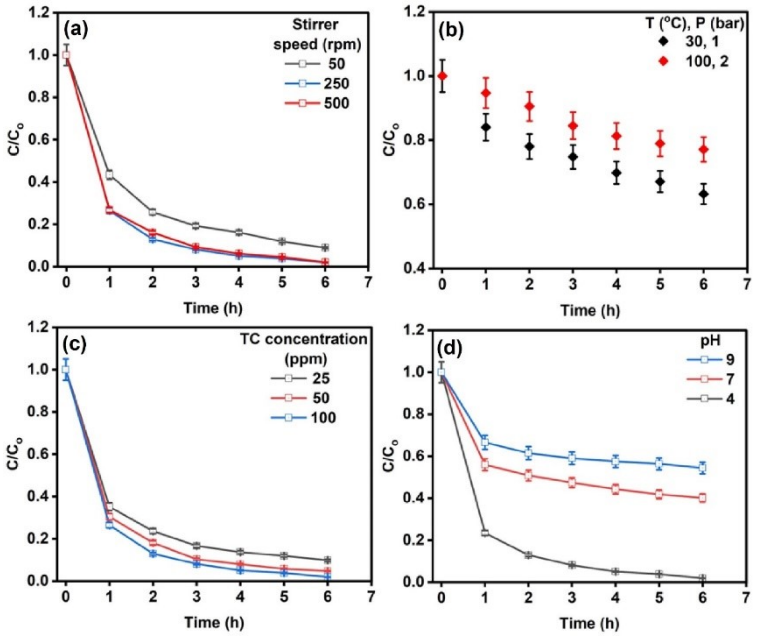

Fig. S13. (a) Effect of stirrer speed on TC degradation (initial concentration = 100 ppm, catalyst dose = 1 g L^{-1}, pH = 4, temperature = 100 °C, pressure = 2 bar), (b) Effect of temperature on TC removal by adsorption (initial concentration = 100 ppm, catalyst dose = 1 g L^{-1}, pH = 4, stirrer speed = 250 rpm), (c) Effect of initial concentration on TC degradation (catalyst dose = 1 g L^{-1}, pH = 4, temperature = 100 °C, pressure = 2 bar, stirrer speed = 250 rpm), (d) Effect of pH on TC degradation (initial concentration = 100 ppm, catalyst dose = 1 g L^{-1}, temperature = 100 °C, pressure = 2 bar, stirrer speed = 250 rpm).

by replacing (oxidant) air with (inert) nitrogen to determine the removal of TC by the synthesized pellets via adsorption. The data revealed ~37% of TC removal via adsorption at room temperature (30 °C) (Fig. S13b). This implies a good adsorption capability of the material attributed to its macroporous structure. The TC removal by adsorption expectedly decreased to ~23% at 100 °C, the combined adsorption and oxidation data revealed that the role of adsorption during cWAO tests was secondary in removing the aqueous TC.

Fig. S13c shows the effect of the initial TC concentrations (25, 50, and 100 ppm) on the TC removal. As shown, the degradation is rapid at relatively higher concentrations owing to a greater mass-transfer rate from the bulk solution to the catalyst surface. Therefore, the percentage degradation of TC decreased with the decrease in the initial concentration, though the final TC concentration remained constant at ~1.5 ppm. Fig. S12d shows the initial pH (4, 7, and 9) effects. The pH value of the TC test solution at 100 ppm was measured to be ~4. The test solutions of high pH (7 and 9) were prepared by mixing 100 ppm -TC solution with required amount of the aqueous NaOH. The oxidation activity data indicates that the maximum conversion (~99%) occurred at pH 4. However, the conversion drastically decreased to ~60 and 43% in the test solution at pH 7 and 9, respectively, clearly indicating that the acidic condition promoted the TC oxidation. The relatively higher rate of degradation at low pH is attributed to the positive potential of $O_2/^{\bullet}O_2^-$ redox couple[5] increasing the reduction of dissolved oxygen and to the stability of generated H_2O_2, responsible for $^{\bullet}OH$ generation[6]. On the other hand, the alkaline condition resulted in a decrease of the reduction potential of O_2 and the decomposition of H_2O_2 to H_2O and O_2 instead of $^{\bullet}OH$ radicals, thus adversely affecting the mineralization of the organic compound.

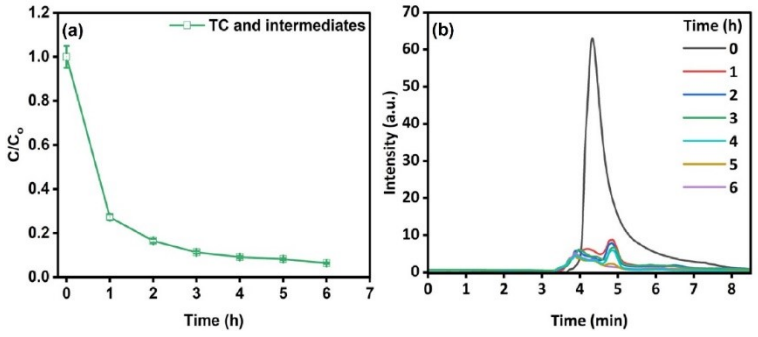

Fig. S14. HPLC analysis (chromatogram) of the cWAO reaction samples: variation in the intensity of TC and intermediates.

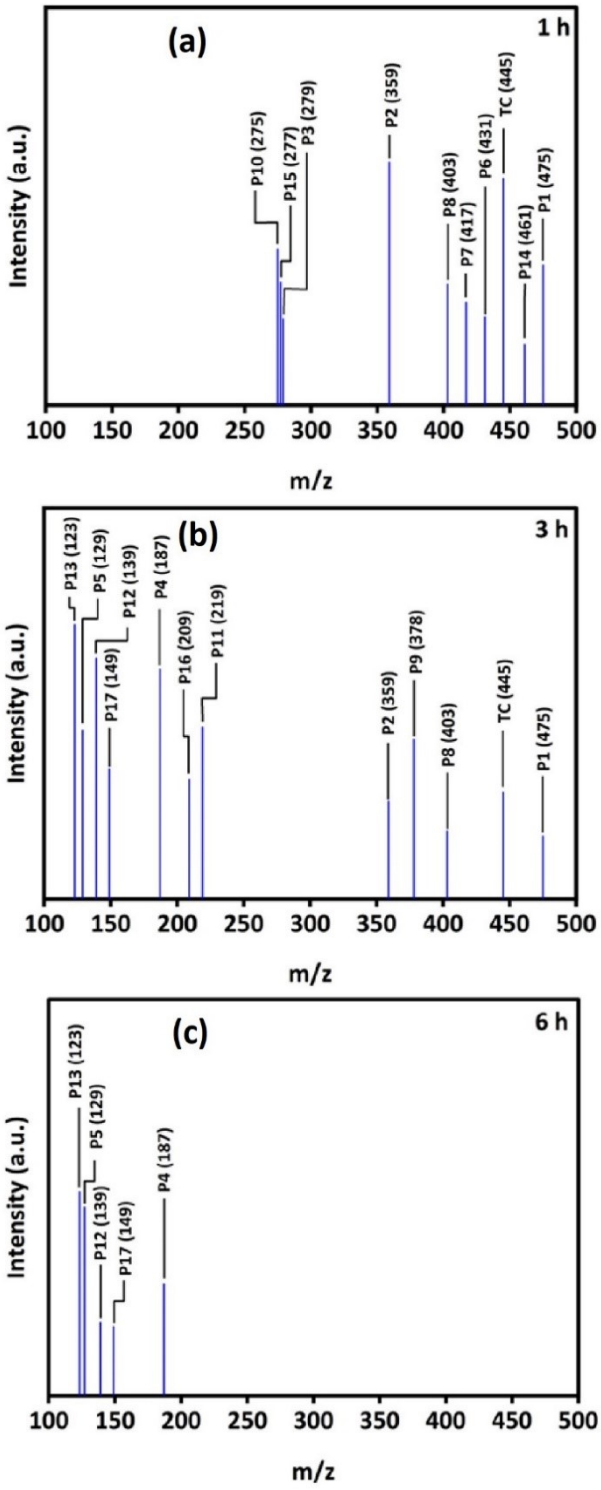

Fig. S15. LC/MS m/z spectra of the cWAO reaction samples collected at (a) 1 (b) 3 and (c) 6 h to determine intermediates.

S3. Reusability and toxicity assay

Additional tests were performed on the spent Cu-CNF/biochar(P) to assess the reusability of the synthesized formulation in this study. After washing the pellets with distilled water, the spent catalyst was dried overnight at 100 °C. The re-cWAO test data showed ~93% TC removal post-five cycles (Fig. S16a). Additionally, the COD analysis was performed for the spent solution post-five cycles of cWAO. The data showed a 74% COD reduction (Fig. S16b). The SEM image of the spent Cu-CNF/biochar catalyst is shown in Fig. S17a. No significant change in the morphology of the material post-the cWAO tests was observed. The EDX analysis showed an increase of the oxygen contents in the spent Cu-CNF/biochar(P) sample, although the percentage of Cu remained approximately constant (Fig. S17b/Fig. 2f). The XRD spectra of the spent sample showed the characteristic peak at 2Θ ~23° corresponding to the (0 0 2) crystal plane of the amorphous carbon (Fig. S17c). The peaks at 2Θ ~ 36.7, and 61.6° correspond to Cu_2O and that at 2Θ ~ 42.5 and 73.7° corresponds to Cu, implying change in the oxidation state of Cu from Cu^0 to Cu^+. Figure S17d presents the XPS survey spectrum of the spent catalyst, where the characteristic signals corresponding to C 1s, N 1s, O 1s, and Cu 2p are clearly observed. Figures S18a-d show the deconvoluted high-resolution spectra for the corresponding regions. The spectral profiles closely resemble those of the fresh catalyst, with no emergence of any new peaks in the C 1s, N 1s, or O 1s regions. This confirms that no new surface functionalities or chemical species are generated on the phenolic resin during the cWAO process. Only minor changes in peak intensities are detected: a slight decrease in C 1s intensity and a modest increase in O 1s intensity, which are consistent with mild surface oxidation during reaction, without alteration of the fundamental chemical structure of the resin. In the Cu 2p region, a small additional peak associated with Cu^{2+} appears, indicating partial oxidation of Cu^0 to Cu^{2+} under cWAO conditions. However, this peak

remains relatively minor (Cu^{2+}/Cu^{0} peak-area ratio ≈ 0.26), confirming that the majority of copper remains in the zero-valent state after reaction. These XPS observations are consistent with the XRD results, which show a reduced intensity of the (0 0 2) carbon diffraction peak and the emergence of Cu_2O diffraction peaks in the spent catalyst. Furthermore, Fig. S19 presents the FTIR spectra after five regeneration cycles, revealing no significant changes in the major vibrational bands of the phenolic resin (aromatic C-H, C-O, and phenolic O-H stretching), indicating a negligible degradation of the chemical moieties in the binder.

Collectively, the XRD, XPS, and FTIR analyses confirm that the phenolic resin retains its chemical stability and structural integrity over five cWAO cycles, with only minor and expected surface-level modifications that do not compromise the performance of catalyst.

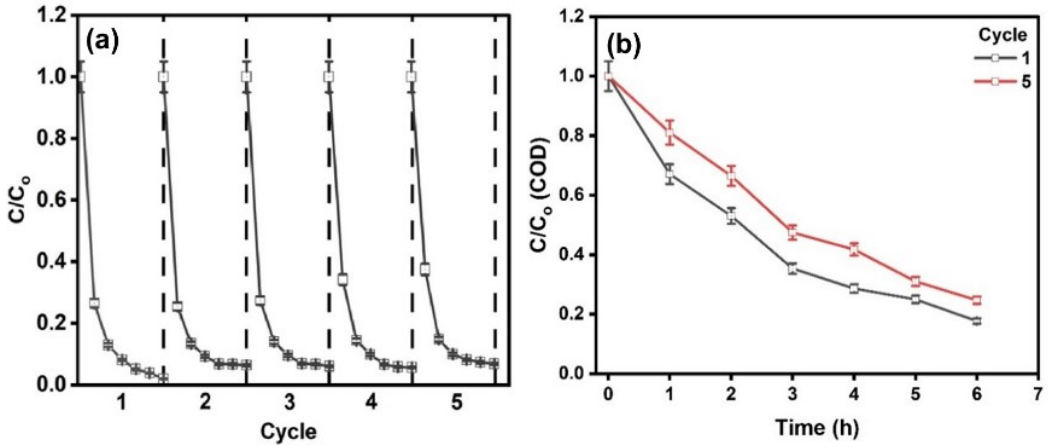

Fig. S16. (a) Recycle test for TC degradation with Cu-CNF/biochar(P) as catalyst (initial concentration = 100 ppm, catalyst-dose = 1 g L^{-1}, pH = 4, temperature = 100 °C, pressure = 2 bar, stirrer speed = 250 rpm) and (b) COD reductions with time for the 1st and 5th cWAO cycle.

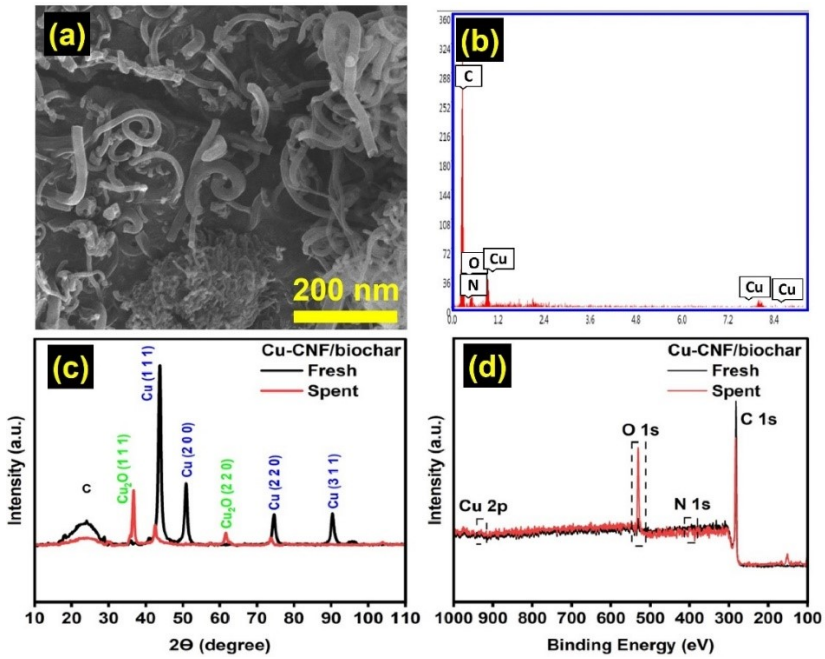

Fig. S17. Cu-CNF/biochar (spent): (a) SEM, (b) EDX spectra, (c) XRD spectra, and (d) XPS spectra.

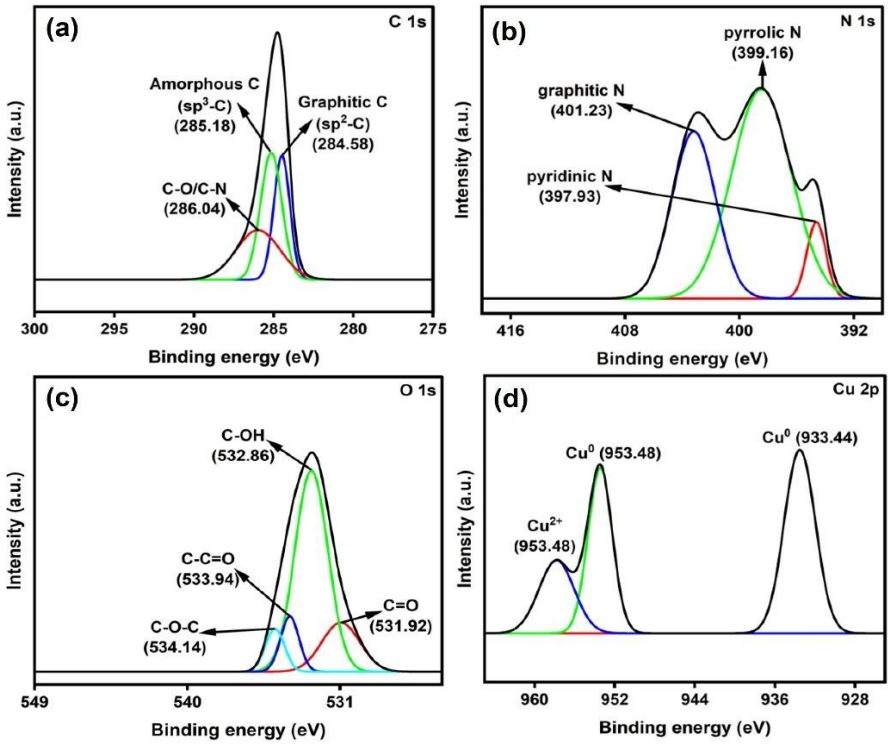

Fig. S18. Elemental deconvoluted XPS spectra of the spent catalyst: (a) C 1s, (b) N 1s, (c) O 1s, and Cu 2p.

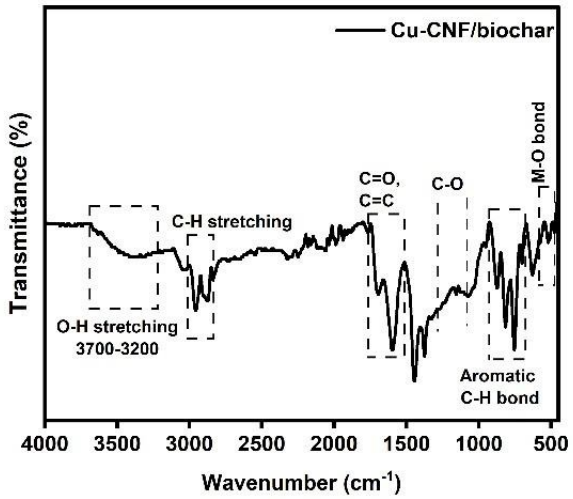

Fig. S19. FTIR spectrum of the spent catalyst.

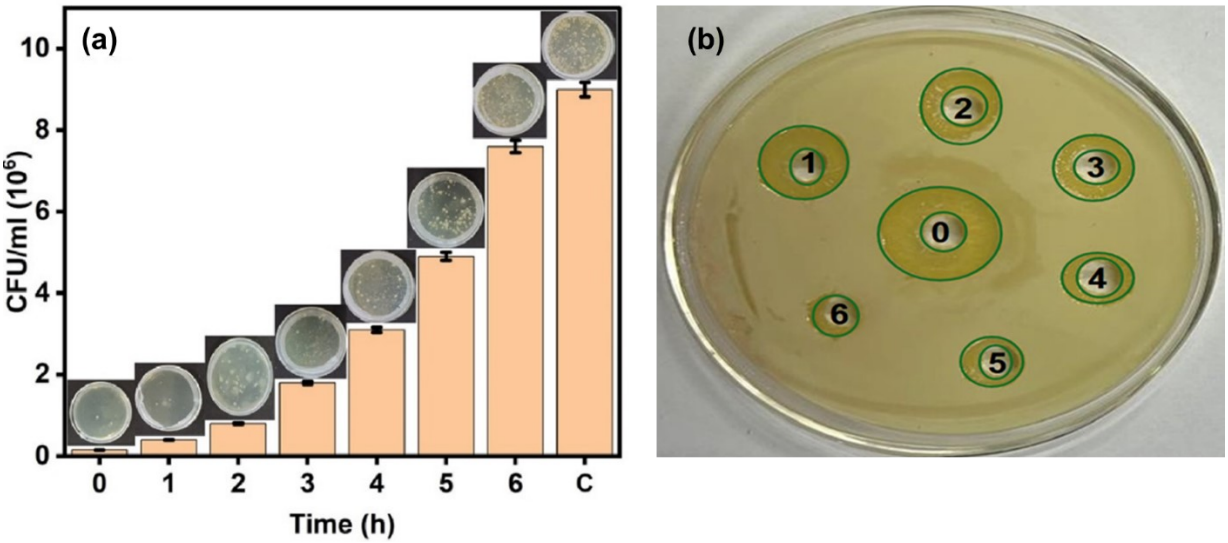

Fig. S20. (a) Digital image and bar plots show bacterial colony growth in the spent liquid, sampled at 1 h intervals during the TC degradation test and (b) zone inhibition microbial test results of the treated cWAO samples.

The plate counting method was used to assess the toxicity of the reaction samples against *Escherichia coli* (E. coli) using LB agar media[7,8]. The samples were collected over 1 h intervals. The media was prepared by mixing 5 g yeast extract, 10 g tryptone, 10 g sodium chloride, and 15 g agar powder in 1 L water. The prepared mixture was sterilized in an autoclave for 1 h. ~100 µL of the bacterial species was inoculated in 100 mL of the autoclaved LB media. The resultant mixture was kept in an incubator for bacterial growth for 2 h at 37 °C under constant stirring at

100 rpm. 100 μL each of the freshly grown *E. coli* and cWAO reaction samples were mixed to prepare the toxicity test solution. The resultant solution was evenly distributed over the prepared agar media poured over the petri plates and left for incubation for 24 h at 37 °C. A control test solution (C) was separately prepared by mixing the freshly grown *E. coli* with the Milli-Q water, and the mixture was incubated under the identical conditions as sued for the cWAO samples. *E. coli* growth in the test samples was determined by counting the number of bacterial colonies.

Fig. S20a shows the results of the toxicity tests. Negligible bacterial growth was observed in the initial reaction samples. The later samples, however, showed an increase in the number of bacterial colonies. The gradual increase in the number is attributed to the decrease in the toxicity of the spent liquid samples over the reaction time, as the aqueous TC degraded to the comparatively lesser toxic reaction intermediates, which were further mineralized to CO_2 and H_2O. The growth of the number of bacterial colonies in the final cWAO test sample is slightly lower than that of the control experiment owing to the presence of residual carbon content. Finally, the pH measurements of the spent (treated) solution showed that pH increased from an initial value of 4 to 4.5 post-mineralization.

The zone inhibition test was performed to assay the toxicity of the treated cWAO samples. *E. coli* bacterial culture was spread on the Mueller-Hinton agar plate of diameter ~8.3 cm. Seven wells of diameter ~0.81 cm were formed using a sterile cork borer. A 100 μL aliquot of each collected sample from the cWAO treated wastewater was added to the wells using micropipettes. The samples were taken every 1 h during the 6 h cWAO test run. The plates were incubated for 24 h in a BOD incubator (Mahendra Inc, Kanpur, India) at 37 °C. The zone of inhibition was measured after incubation. Seven samples, comprising the feed (#0) and the hourly collected samples (#1-6), were added to the corresponding wells as shown in Fig. S20b. The diameter corresponding to the

inhibition-zone was measured for each well. A clear decreasing trend in the diameter of inhibition-zone including well diameter was observed from the feed sample to the final 6 h-sample. The recorded diameters for 0 (feed), 1, 2, 3, 4, 5, and 6 h were 2.01 ± 0.1, 1.56 ± 0.08, 1.40 ± 0.07, 1.17 ± 0.06, 1.14 ± 0.06, 0.99 ± 0.05, and 0.81 ± 0.04 cm, respectively. No inhibition zone appeared in the 6 h-sample. The bacterial colony count test showed the same pattern. The decrease in inhibition-zone diameter and the increase in colony count are attributed to the reduction in toxicity level as the reaction progressed. Aqueous TC gradually degraded to less-toxic intermediates, which were further mineralized to CO_2 and H_2O.

Table S1. Total moles of O_2 supplied to the reactor at different temperature and pressure conditions. The theoretical value* for the required amount of oxygen (COD) is calculated based on the complete mineralization of TC at 100 ppm, i.e. the maximum concentration used in the study.

Pressure (bar)	T (°C)	Total moles of O_2 supplied/available	% excess O_2
1	40	4.54×10^{-3}	1957
	70	4.14×10^{-3}	169
2	100	7.62×10^{-3}	395
5	40	2.27×10^{-2}	1376
	70	2.07×10^{-2}	1247
	100	1.90×10^{-2}	1138
	150	1.68×10^{-2}	992

Sample calculation (for the reaction at 150 °C and 5 bar):

*Moles of O_2 required to completely mineralize TC at 100 ppm (R_{O2}) = $\frac{COD \times V}{M \times 10^6} = 1.54 \times 10^{-3}$
where, COD of TC at 100 ppm = 164 mg/L, volume of the reaction mixture (V) = 300 mL, M = molecular weight of O_2 = 32 g/mol.

Total moles of O_2 supplied (N_{O2}) = $\frac{0.21 \times P \times V_R}{R \times T} = 1.68 \times 10^{-2}$

% excess O_2 supplied = $\frac{N_{O_2} - R_{O_2}}{R_{O_2}} \times 100 = 992$

where, P = pressure in the reactor; V_R = volume of empty (vapor) space over the reaction mixture in the reactor; R = gas constant; T = reactor temperature

Thus, the data clearly show an excess of oxygen was maintained throughout the reaction under all operating conditions.

Table S2. Mass transfer coefficient calculated at different stirrer speeds.

Stirrer speed (rpm)	Reynolds number (Re)	Schmidt number (Sc)	Sherwood number (Sh)	Mass transfer* coefficient (m/sec)
50	28	2433	108	2.62×10^{-5}
250	139	2433	281	6.79×10^{-5}
500	278	2433	424	1.03×10^{-4}

*Diffusion coefficient of TC at 100 °C and 2 bar = 1.21×10^{-10} m^2 sec^{-1}

Diameter of the pellet = 5 mm
Kinematic viscosity of water at 100 °C and 2 bar = 2.94×10^{-7} m^2 sec^{-1}
$Sh = 2 + 1.1 \times Re^{0.6} \times Sc^{0.33}$; $3 < Re < 3000$ (Gupta et al., 1998)

Table S3. Parameters of the kinetic rate model at various temperatures (°C) (m = 0.06, n = 0.1307)

T (°C)	k (L/min-(g of cat)^n -(bar)^m)	K_{ads} (M^{-1})	R^2
40	0.062	0.132	0.948
70	0.137	0.131	0.965
100	0.243	0.129	0.991

Table S4. Comparative analysis of the performance of different catalysts including biochar supported with/without metals for TC removal.

S.No	Method	Caytalyst	C_o (ppm)	T(°C) ,P (bar)	Dose (g L^{-1})	Time (h)	Removal (%) TC/ COD/TOC	Kinetics (reaction-order)	Rate constant	E_a (kJ mol^{-1})	Toxicity (Y/N)	Ref.
1	cWAO	Cu-CNF/ biochar(P)	100	100, 2	1	6	~99/78/80	$\frac{kCP_{O_2}^{m}W_{cat}^{n}}{(1+K_{ads}C)^2}$	0.243 L/min-(g-cat)^n -(bar)^m	9.62	Y	This study
2	cWAO	Pt/Ce, Pt/CeZr	200	50, 1	4	3	~98/-/~98	-		-	Y	9
3	cWAO	Cu_x-g-C_3N_4	2100	120, 10	1	1	97/-/-	-		-	N	10
	Biochar (with/without metal catalysts)											
4	Oxidation	Passion fruit shell char (PMS)	20	30, 1	0.4	2	91/-/61	2nd order	0.0317 $L{\cdot}mg^{-1}{\cdot}min^{-1}$	-	Y	11
5	Oxidation	N-doped bamboo biochar (PMS)	50	25, 1	0.2	1	94/-/53			-	Y	1
6	Oxidation	N-Cu/glucose derived biochar (PS)	200	25, 1	0.2	2	96/-/26	1st order	0.0482 min^{-1}	-	Y	12
7	Oxidation	$CuFeO_2$/ pepper stalk derived biochar (H_2O_2)	20	25, 1	0.5	5	88/-/58			-	Y	13
9	Oxidation	Mn- bamboo derived biochar (PS)	20	25, 1	0.2	3	93/-/70	1st order	0.0267 min^{-1}	-	N	14
10	Oxidation	$MgFe_2O_4$/ banana stem derived biochar	30	25, 1	0.8	1.5	95/-/63	1st order	0.0288 min^{-1}	-	Y	15

		(PDS)										
11	Oxidation	Co_2P/ Neosinocalamus afinis biochar (PMS)	50	25, 1	0.2	0.5	99/-/68	1st order	0.1496 min^{-1}	-	N	16
	Non-biochar carbon-supported catalysts											
12	Oxidation	Microplastics-derived B-N-doped carbon (PMS)	20	25, 1	0.13	1	94/-/55	2nd order	0.228 L $(mg\text{-}min)^{-1}$	-	N	17
13	Oxidation	MOF-derived ZVI-carbon (H_2O_2)	40	25, 1	0.04	0.167	81/-/-	1st order	0.299 min^{-1}	22	N	6
14	Oxidation	N-graphite carbon (PDS)	20	25, 1	0.05	3	94/-/70	1st order	0.041 min^{-1}	-	Y	(Pi et al., 2022)

* PS: Persulfate; PMS: Peroxymonosulfate; PDS: Peroxydisulfate

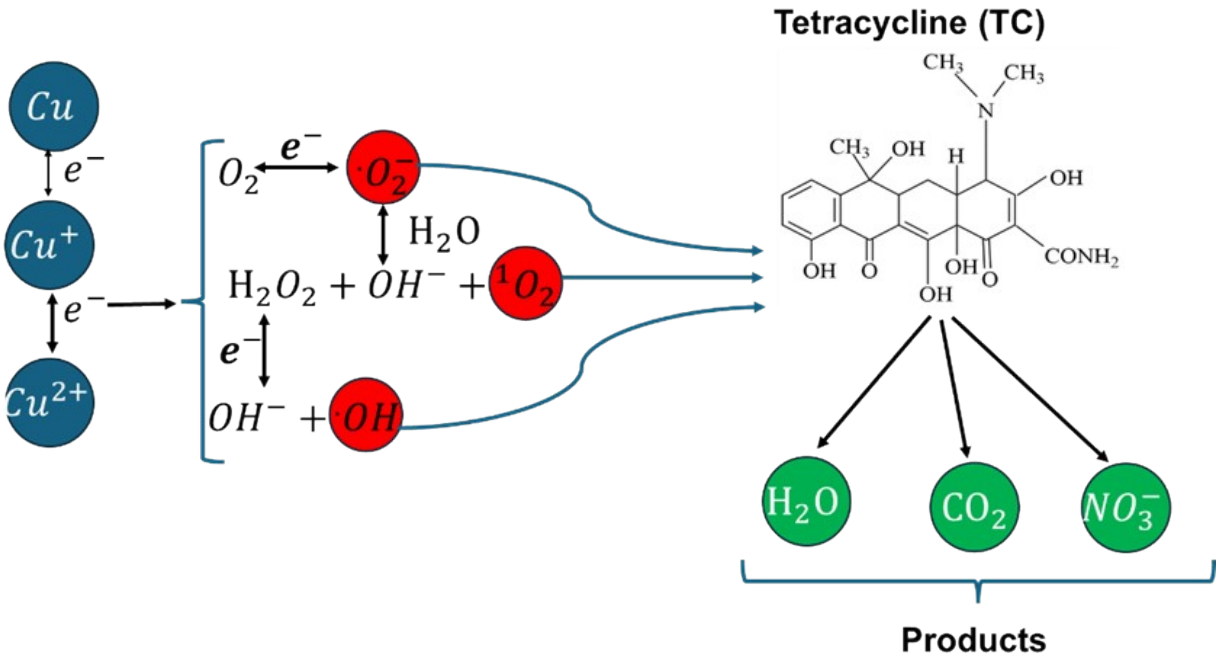

Scheme 1S: Proposed electron-transfer model demonstrating the synergistic ROS-generation process during cWAO.

References

1 X. Huang, F. Li, X. Zhang, S. Xu, H. Liu, C. Qiu, Y. He, M. Li, Y. Jiang, S. Jia, C. F. de Hoop, Y. Chen, J. Qi and X. Huang, One-step high-efficiency microwave synthesis of N-doped bamboo biochar for tetracycline degradation Sep. Purif. Technol., 2025, 354, 129003.

2 H. Wang, W. Guo, B. Liu, Q. Wu, H. Luo, Q. Zhao, Q. Si, F. Sseguya and N. Ren, Edge-nitrogenated biochar for efficient peroxydisulfate activation: An electron transfer mechanism Water Res., 2019, 160, 405–414.

3 K. Zhu, Q. Bin, Y. Shen, J. Huang, D. He and W. Chen, In-situ formed N-doped bamboo-like carbon nanotubes encapsulated with Fe nanoparticles supported by biochar as highly efficient catalyst for activation of persulfate (PS) toward degradation of organic pollutants. Chem. Eng. J., 2020, 402, 126090.

4 A. Kumar and N. Verma, Cu-Fe bimetal-carbon nanofiberous catalytic beads for enhanced oxidation of dichlorvos pesticide and simultaneous reduction of Cr(VI) in wet air. Catal. Today, 2020, 348, 194–202.

5 Z. Zhou, Z. Shen, C. Song, M. Li, H. Li and S. Zhan, Boosting the activation of molecular oxygen and the degradation of tetracycline over high loading Ag single atomic catalyst. Water Res., 2021, 201, 117314.

6 R. Sun, J. Yang, R. Huang and C. Wang, Controlled carbonization of microplastics loaded nano zero-valent iron for catalytic degradation of tetracycline. Chemosphere, 2022, 303, 135123.

7 A. Kumar and N. Verma, Wet air oxidation of aqueous dichlorvos pesticide over catalytic copper-carbon nanofiberous beads. Chem. Eng. J., 2018, 351, 428–440.
8 P. Gupta and N. Verma, Evaluation of degradation and mineralization of glyphosate pollutant in wastewater using catalytic wet air oxidation over Fe-dispersed carbon nanofibrous beads. Chem. Eng. J., 2021, 417, 128029.
9 M. Bourassi, G. Lafaye, B. Gombert, P. Klusoň and J. Barbier, Catalytic wet air oxidation of sulfamethoxazole and tetracycline using platinum-based catalysts at eco-operating conditions. J. Clean. Prod., 2023, 429, 139453.
10 W. Zhang, B. Ye, Z. Zhong, Y. Jiang, R. Zhou, Z. Liu and Z. Hou, Catalytic wet air oxidation of toxic containments over highly dispersed Cu(II)/Cu(I)-N species in the framework of g-C3N4. J. Hazard. Mater., 2022, 424, 127679.
11 Y. Hu, D. Chen, R. Zhang, Y. Ding, Z. Ren, M. Fu, X. Cao and G. Zeng, Singlet oxygen-dominated activation of peroxymonosulfate by passion fruit shell derived biochar for catalytic degradation of tetracycline through a non-radical oxidation pathway. J. Hazard. Mater., 2021, 419, 126495.
12 Q. Zhong, Q. Lin, R. Huang, H. Fu, X. Zhang, H. Luo and R. Xiao, Oxidative degradation of tetracycline using persulfate activated by N and Cu codoped biochar. Chem. Eng. J., 2020, 380, 122608.
13 S. Xin, G. Liu, X. Ma, J. Gong, B. Ma, Q. Yan, Q. Chen, D. Ma, G. Zhang, M. Gao and Y. Xin, High efficiency heterogeneous Fenton-like catalyst biochar modified CuFeO2 for the degradation of tetracycline: Economical synthesis, catalytic performance and mechanism. Appl. Catal. B, 2021, 280, 119386.
14 D. Huang, Q. Zhang, C. Zhang, R. Wang, R. Deng, H. Luo, T. Li, J. Li, S. Chen and C. Liu, Mn doped magnetic biochar as persulfate activator for the degradation of tetracycline. Chem. Eng. J., 2020, 391, 123532.
15 L. Wang, X. Lu, G. Chen, Y. Zhao and S. Wang, Synergy between MgFe2O4 and biochar derived from banana pseudo-stem promotes persulfate activation for efficient tetracycline degradation. Chem. Eng. J., 2023, 468, 143773.
16 Z. He, Y. He, F. Chang, Z. Li, J. Niu, M. Li, S. Zhang, X. Li, R. Shi and G. Hu, Efficient pH-universal degradation of antibiotic tetracycline via Co2P decorated Neosinocalamus affinis biochar. Chemosphere, 2022, 286, 131759.
17 J. Xie, L. Chen, X. Luo, L. Huang, S. Li and X. Gong, Degradation of tetracycline hydrochloride through efficient peroxymonosulfate activation by B, N co-doped porous carbon materials derived from metal-organic frameworks: Nonradical pathway mechanism. Sep. Purif. Technol., 2022, 281, 119887.
18 Z. Pi, K. Hou, F. Yao, L. He, S. Chen, Y. Fu, X. Li and Q. Yang, Nonradical-dominated peroxydisulfate activation by nitrogen-rich hierarchical porous graphite carbon for efficient degradation of tetracycline. Carbon N Y, 2022, 196, 736–748.